Research Article

Effects of Splitting Airfoil's Aspect Ratio on the Control of Separation and Loss Distribution in a Distortion Generator

M. Hassani (ID), **M. Bazazzadeh** (ID), **and M. D. Manshadi** (ID)

Mechanical Engineering Faculty, Malek-Ashtar University, Esfahan, Iran

Correspondence should be addressed to M. Bazazzadeh; bazazzadeh@mut-es.ac.ir

The effects of aspect ratio (AR: opposite diameter to width) reduction on the total pressure loss distribution of horizontally arranged splitting airfoils are investigated experimentally and numerically. The array arrangement of airfoils is proposed as a novel distortion generator mechanism. The upgrade feasibility study of the single airfoil loss repeatability in combined pattern was the aim of the present research. Modification of 90° splitting airfoil as a representative of the airfoils category with AR > 1 was a corrective approach to eliminate or delay the downstream wake axis rotation destructive effects on the combined loss predictability. The results of the modified airfoil (single and multiple arrangements) wake simulations based on hybrid turbulence model demonstrate a good agreement with wind tunnel measurements. It was observed that the aspect ratio reduction below the limiting value of "1" for selected opening angle provides the quasi-2D behavior of downstream flow structure related to AR < 1 airfoil category along with relatively higher value of loss related to AR > 1 category. Elimination of the side separation for modified 90° airfoil and the resulting similarity of maximum loss lobes positioning in arrangement of airfoils lead to the reduction of combined flow structure complexity and the improvement of loss predictability. It has appeared that combined loss pattern of the triple arrangement of the airfoils can be reconstructed from dual arrangement, and it can be reproduced from a single pattern in a hierarchical process. Concerning the maximum loss coefficient "values," an overprediction of velocity recovery rate was observed in simulation results at the fully developed wake region that led to approximately 15% lower maximum loss values in comparison with the experiments.

1. Introduction

The aerodynamic compatibility of an airframe-propulsion integrated system is an important aspect of aircraft design and development process that is determined using various experimental and computational tools. Thus, the quality of delivered flow by inlet (to the engine) is evaluated by the identification of nonuniformities in the distribution of flow properties at engine face, by which the resulting performance and stability variations are evaluated [1, 2]. The total pressure distortion is the most commonly encountered type, and it also has the most deteriorating effect on the compressor performance [3]. With the inlet total pressure distortion, the compressor pressure ratio falls compared with the ideal inlet condition [4]. Calculating these effects on a combat aircraft equipped with embedded engine subjected to varying degrees of distortion during maneuver flight at high flight angles is a critical step in the design process [5]. High levels of pressure distortion are present due to the combined influence of the ingestion of the airframe boundary layer and the generation of secondary flows by the intake [6].

Ground testing and flight test are two main categories of engine test resources. Ground testing that includes large propulsion wind tunnel test and direct-connect test technique plays a critical role in the vehicle development cycle by providing needed information early enough to reduce the overall project cost and risk [2]. Through a direct-connect test technique, distortion generation is the most widely used method for determining the inlet-engine compatibility before manufacturing the main inlet. The inlet simulator channel employs distortion generators to provide the engine with replicated patterns of inlet distortion. The final phase of the engine distortion analysis allows the determination of acceptable levels of flow distortion [7].

Inlet-engine compatibility researches concentrated on steady distortion, during the early decades. Flight tests of F-111 aircraft powered by TF30 engines confirm the possibility of encountering higher time-dependent distortion levels and their more severe effects coexisting with tolerable steady-state distortion values [8]. In this regard, the approach to distortion generation research has shifted away from traditional steady-state distortion generators (such as distortion screens described in Ref. [1]) toward new designs capable of producing time-dependent distortion, one of which is the array mechanism described in the presented research. Numerous designs have been proposed over the years, including the random frequency generator of Younghans et al. [9], the separate frequency generator of Lazalier and Tate [10], and the research on screen wave generator by Kutschenreuter et al. [11]. Following the experimental studies of DiPietro [12] and Jumel et al. [13] on splitting airfoils as a total pressure distortion generator, Eddy Jr. [14] measured the effect of the airfoil aspect ratio (AR) on the structure of the downstream flow and demonstrated that, after a specific downstream station, the wake axis of a splitting airfoil with AR > 1 changes from a vertical configuration (lobes of maximum total pressure loss on top of each other) to a horizontal layout (lobes of maximum loss stacked next to one another).

Possibility of varying the airfoil opening angle is the distinct advantage of the present distortion generation mechanism which can lead to producing a distortion time history. Before addressing the unsteady effects, it is necessary to extract the relationship between each array configuration parameter and the resulting combined loss distribution and evaluate its reproducibility and controllability. Repeatability studies of a single airfoil loss pattern in multiple arrangement pattern revealed that wake axis switching (from vertical to horizontal) is a destructive factor for combined pattern predictability.

The present study investigated the effects of reducing the aspect ratio of 90° airfoil (as a representative of the airfoils category with AR > 1) below the limiting value of "1" on the downstream flow structure and wake combination pattern of multiple airfoils arrangement. The ratio of airfoil opposite diameter to its width has been changed to correct the destructive effects of wake axis rotation on pattern predictability. The combined loss distribution has been compared for 2 categories of combinations: (1) standard airfoil arrangements and (2) modified airfoil arrangements. Numerical simulations were carried out based on the delayed detached Eddy simulation hybrid turbulence model that captures the downstream wake axis switching by resolving the separated shear layers in LES mode. Along with simulations, total pressure loss due to the splitting airfoils arrangement has been measured in wind tunnel at lateral sections of the flow field especially in far wake region. The experiments were conducted to validate the effect of aspect ratio variation on the array distortion character obtained from simulations. This is a critical step in creating an array mechanism that exhibits a predictable loss pattern. In several instances throughout this paper, the term "wedge" is used instead of "splitting airfoil."

## 2. Statement of the Problem and Methods

The splitting airfoil aspect ratio variation effects on the single and combined loss distribution were studied at downstream stations (station 1 at 25.4 mm from the axis to station 9 with fixed longitudinal step equals to 50.8 mm between stations). The resulting flow structure and wake patterns have been investigated with numerical and experimental tools. The results of single airfoil's flow simulation demonstrated that rotation of maximum loss lobes positioning for airfoils with aspect ratio greater than 1 is a challenge to predict the combined pattern from singles. Considering Eddy Jr.'s experimental tests [14], the effects of aspect ratio reduction below the value of "1" for 90° wedge has been studied using 3 modified variants described in Figure 1 and Table 1. This airfoil belongs to the category of airfoils with AR > 1 (AR: OD to s, Figure 1(a)). In addition, the opening angle effect at the determined AR has been analyzed numerically and experimentally through the "60new" modified airfoil. Wind tunnel measurements have been conducted on selected airfoil arrangements due to the multiplicity of configuration parameters such as airfoils aspect ratio, angles, spacing, among others, and the resulting costs of experiment.

Numerical simulation of all modified variants flow field was performed separately to study the elimination or delaying of wake axis switching and selection of 1 variant for arrangements. Loss distribution of airfoils horizontal arrangement including selected modified wedge has been simulated to compare the corrective approach effects on combined loss pattern.

Concerning wind tunnel tests, it should be noted that total pressure loss measurements were made by scrolling the rake of pitot tubes at selected stations (lateral sections perpendicular to the tunnel flow) located from the near to far wake region of the downstream flow. A comparison of the resulting loss distribution to the simulation results was performed. The critical parameter is the total pressure loss coefficient, denoted by the abbreviation "cp," which is defined as follows:

$$cp = \frac{p_{t\,\max} - p_t}{p_{t\,\max}} \times 100. \tag{1}$$

2.1. Computational Grid Considerations. The present research used Ansys Fluent and the "finite volume" method to solve the governing equations. It is critical to select the appropriate turbulence model and provide a suitable computational grid for the selected model [15]. In the downstream zone of a typical bluff body, which is the concentration region of the present study, the flow is unaffected by the wall. At the short distance from the wall, the separated free shear layers form the boundaries of the near wake separation bubble, which is composed of recirculating flow. This entire area behind the body is referred to as the wake that is going to fully development as it goes to downstream [16, 17]. One of the most compatible turbulence models with the described downstream flow structure from the RANS family is $k\omega$ [15]. Significant differences in the amount and the trend of cp variation obtained from steady-
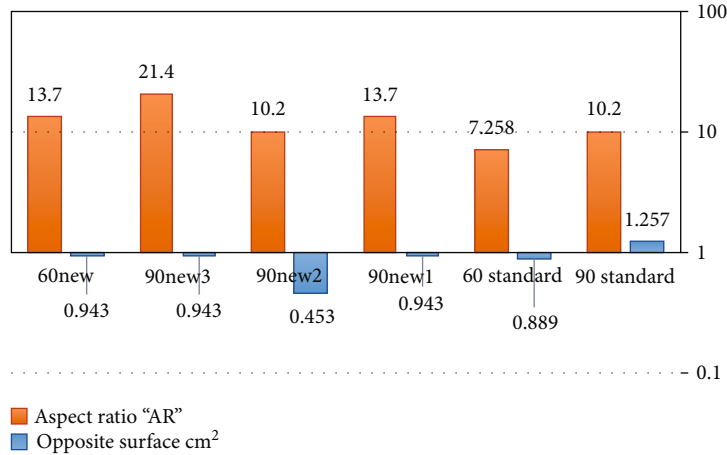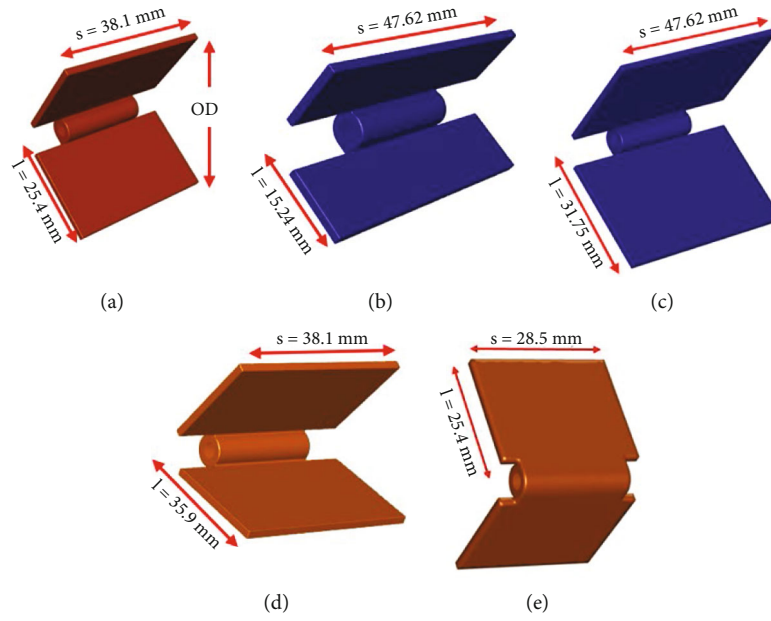
Figure 1: Modified AR variants of splitting airfoil. (a) 90new1. (b) 90new2. (c) 90new3. (d) 60new. (e) 90° standard. (f) AR and S_{op} values.

Table 1: Design characteristic of modified aspect ratio variants.

Test case No.	Designation	Purpose of standard airfoil resize
1	90new1	Study of aspect ratio reduction below limiting value of "1"
2	90new2	Study of further reduction of aspect ratio relative to the test case No. 1
3	90new3	Study of opposite surface increase at equal aspect ratio relative to the test case No. 1
4	60new	Study of opening angle reduction at equal aspect ratio relative to the test case No. 1

state simulation were observed in comparison to the reference experiments [14]. Transmitting the applied $y+$ requirements on the walls to the downstream zone of flow was not useful to improve the results.

2.1.1. Grid Refinement Based on the Physics of Flow. According to a literature review, one of the determining factors in the fundamental characteristics of flow passing through the

bluff bodies is the pattern of vortex formation and shedding. As per Ref. [18], the downstream flow structure of the geometry studied in this research belongs to the family of sharp-cornered sections with considerable curvature (e.g., square and triangular cylinders). The Reynolds number has little effect on the flow structure for the category as mentioned above because the separation point is fixed at the sharp (top and bottom) edges [19]. The performance of the vortex
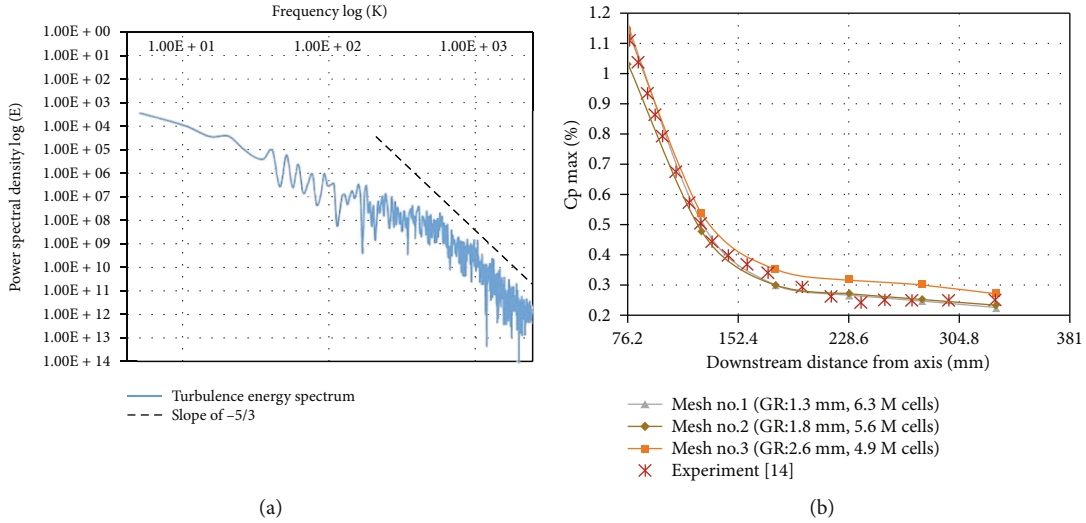
(a)

(b)

FIGURE 2: (a) Power spectral density obtained by current DES results on finest grid zone to study the Kolmogorov's −5/3 scale law requirements. (b) Solution-grid independency study conducted on the single 90° airfoil.

depends on its dimensions and shedding frequency calculated using the Strouhal number (Equation (2)) [20, 21].

$$St = \frac{f \cdot D}{U}. \tag{2}$$

Taylor [22], Roshko [23], and Cantwell and Coles [24] research in the field of St and Re relationship indicate that the choice of $St = 0.2$ for a 90° splitting airfoil in freestream velocity of 42 m/sec ($Re_{OD} = 1 \times 10^5$) appears reasonable and appropriate; thus, the vortex shedding period is equal to 4.28 $\times 10^{-3}$ sec, and dividing each period by 30 steps, the time step size for unsteady simulation is calculated 1.428×10^{-4} seconds. Estimation of the cell "convective courant number" as a suitability criterion for the chosen time step reveals an allowable range of values less than 40 [15].

Experimental results of total pressure loss measurements indicate that the wake is vertical up to station 5 (228.6 mm from the airfoil axis); after that, the pattern becomes horizontal due to the rotation of the maximum loss lobes' placement and becomes completely horizontal at station 7 (330.2 mm from the axis; entrance of fully developed wake region) [14].

The results of the unsteady simulation with the calculated time step based on $k\omega$-sst turbulence model indicated that the time-averaged distribution of cp at the seven stations was not significantly different from the steady-state solution and was ineffective at predicting wake axis switching. The sampling of P_t loss instantaneous values for time averaging started after giving a respite of at least 5τ to the solution process and a minimum length of 5τ for sampling interval.

The detached Eddy simulation turbulence model was chosen from the SRS category to obtain more information about the flow structure than RANS models offer and to achieve higher accuracy. This hybrid RANS-LES model has been developed to model the connected boundary layer in RANS mode and then switch to LES mode for the separated shear layers (as a solution to avoid from the classical LES computa-

tional costs) [15], which is perfectly consistent with the physics of the present study. Grid refinement within attached boundary layers can activate the LES mode of the DES model resulting in grid-induced separation by lowering the Eddy viscosity. The DDES model extended by Spalart et al. [25] introduces a delayed function to protect the attached boundary layer [26].

2.1.2. Grid Independency. Kolmogorov's -5/3 scale law has been approved for grid generation to apply the solution-grid independency and the requirements of the selected turbulence model [27]. Figure 2(a) demonstrates the turbulence energy spectrum versus wave number proportional to vortex characteristic size obtained by applying the fast Fourier transform to the root mean square of the sampled streamwise velocity fluctuations. The sampling point was located on the vicinity of airfoil's wall at downstream, outside of the boundary layer where the flow turbulence and mesh density were at the highest level. The conformity of the curve slope to the desired value was checked and confirmed. Figure 2(b) compares the variation of cp_{max} at downstream stations for 3 different grid densities passed the Kolmogorov's criterion. Higher mesh resolution and grid numbers obtained by reducing growth rate (GR) of nodes spacing (meshes 1 and 3 have the most and the least number of cells, respectively). In order to balance the accuracy and computational costs, mesh 2 (GR = 1.8) with 5.6 million cells was selected.

Detailed prediction of turbulent mixing downstream of 90° standard airfoil's geometry through the application of DDES turbulence model and its computational grid requirements led to capture the wake axis switching, as compared to the persistence of maximum loss lobes vertical positioning in contours of mean cp at station 7 using the $k\omega$-sst model in Figure 3. According to the appropriate results, the flow field simulation passing through the single modified airfoils was performed to choose the best variant for multiple arrangements. Dual and triple layouts of coaxial airfoils' flow structure including the selected modified 90° airfoil with the same
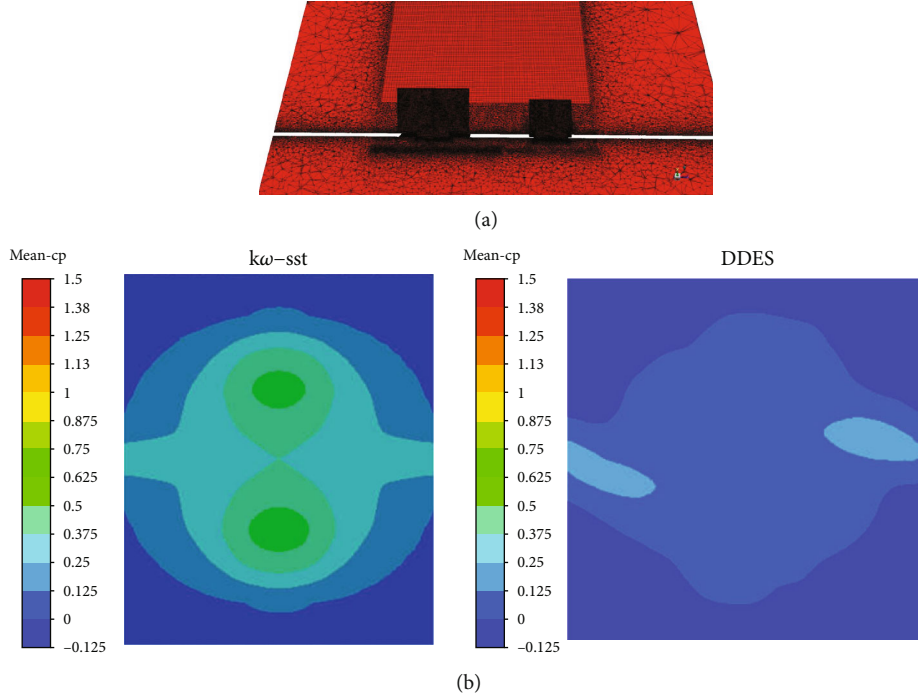
(a)

(b)

FIGURE 3: (a) Final computational grid for arrangement of 90new3-30 with DES model requirements illustrated on horizontal plane. (b) Comparison of DDES and $k\omega$-sst-based numerical simulations to capture the 90° standard airfoil wake axis switching illustrated as time-averaged cp contours at station 7.

preprocessing features was simulated. Grid studies using validated parameters resulted in a hybrid topology as depicted in Figure 3(a) for dual arrangement: one structured and 3 unstructured blocks with an approximately total cell count of 9.8 million. The similar topology was used in triple layouts such as 60-90new3-60 which led to the computational grid with more than 14 million cells.

2.2. Governing Equations. Scale-resolving simulation turbulence models such as DDES were made to obtain additional information not available from RANS models. Spalart [28] introduced detached eddy simulation to overcome the LES model's primary limitations. The formulation is relatively straightforward mathematically and can be applied to any RANS turbulence model. Large Eddy simulation separates the velocity field into the resolved and subgrid parts. The resolved portion of the field corresponds to the "large eddies," whereas the subgrid part corresponds to the "small scales," whose effect on the resolved field is captured by the SGS model. The Navier-Stokes equations are filtered using this technique. When the Navier-Stokes equations are filtered, the following form is obtained (ρ fluctuations neglected):

$$\frac{\partial \rho \bar{U}_i}{\partial t} + \frac{\partial \rho \bar{U}_i \bar{U}_j}{\partial x_j} = -\frac{\partial P}{\partial x_i} + \frac{\partial}{\partial x_j}\left(\bar{\tau}_{ij} + \tau_{ij}^{LES}\right). \quad (3)$$

P denotes static pressure, and τ_{ij} denotes the stress tensor. The equations feature an additional stress term: "τ_{ij}^{LES}" due to the filtering operation.
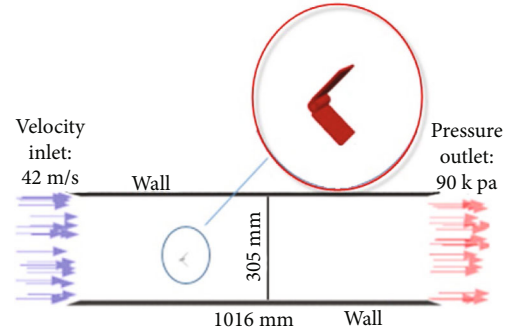

FIGURE 4: Boundary conditions and computational domain schematic illustrated for single airfoil.

Despite the difference in derivation, the additional subgrid stress tensor is typically modeled as in RANS using an Eddy viscosity model:

$$\tau_{ij}^{LES} = \mu_t \left(\frac{\partial \bar{U}_i}{\partial x_j} + \frac{\partial \bar{U}_j}{\partial x_i}\right). \quad (4)$$

μ_t denotes turbulent viscosity. Classical LES models are of the form of the Smagorinsky model [29]:

$$\mu_t = \rho (C_s \Delta)^2 S, \quad (5)$$

where Δ represents a measure of the grid spacing of the numerical mesh, and C_s is a constant. The switch between

(a)

(b)

FIGURE 5: (a) Test section, traverse mechanism, and model located on the ring-shaped stand. (b) The rake of *Pt* probes and splitting airfoils arrangement (close-up).

RANS and LES is made within DES models based on a criterion such as

$$C_{DES}\Delta_{\max} \rangle L_t \longrightarrow RANS$$

$$C_{DES}\Delta_{\max} \leq L_t \longrightarrow LES \tag{6}$$

$$\Delta_{\max} = \max\left(\Delta_x, \Delta_y, \Delta_z\right),$$

where $\Delta_{\max}$ denotes the maximum edge length of the local computational cell. As the grid is refined below the limit $\Delta_{\max} \leq L_t$, the DES-limiter is activated and switches the model from RANS to LES mode [24]. The actual formulation for a two-equation model is as follows (e.g., k-equation of the $k - \omega$ model):

$$\frac{\partial \rho k}{\partial t} + \frac{\partial \rho \bar{U}_j k}{\partial x_j} = P_k - \rho \frac{k^{3/2}}{\min\left(L_t, C_{DES}\Delta_{\max}\right)}$$

$$+ \frac{\partial}{\partial x_j}\left(\left(\mu + \frac{\mu_t}{\sigma_k}\right)\frac{\partial k}{\partial x_j}\right)L_t \tag{7}$$

$$= \frac{k^{3/2}}{\varepsilon} = \frac{\sqrt{k}}{\beta^* \omega}.$$

References [28–30] provide additional information on DES formulations. The DDES and its formulations are discussed in detail in Ref. [31].

2.3. Boundary Conditions and Numerical Models. The solution was performed by a pressure-based double-precision solver that employs a "simple" pressure-velocity coupling scheme and a "bounded second-order" transient formulation. The momentum equation was also discretized using the "bounded central differencing" scheme. Figure 4 shows the computational domain of the present numerical simulation (side view) and applied boundary conditions. The channel width, height, and length are set to 305 mm, 305 mm, and 1016 mm, respectively. The boundary conditions of "velocity inlet" and "pressure outlet" were applied to inlet and outlet planes, as depicted with arrows in the figure. The velocity magnitude is set to 42 m/sec in inlet boundary, according to Eddy Jr.'s wind tunnel tests [14]. Based on the

TABLE 2: The uncertainty for measured total pressure.

Parameter	Uncertainty value
Data acquisition board	0.0001
Calibration mechanism (estimation of repeatability)	0.01
Curve-fitting	0.02
Positional error	
Rake	0.00015
Wedge axis	0.003

no-slip condition, upper and lower wall velocities were considered to be zero.

2.4. Experimental Setup. The closed-circuit low subsonic wind tunnel of Sattari University has been used to conduct the experimental tests of the present research. The tunnel has a cylindrical open test section with the length of 80 cm and the base diameter of 55 cm. The averaged turbulence intensity across the test section was determined about 0.3%. A free stream velocity of 42 m/s was used in all measurements, which corresponds to $Re_{OD} = 1 \times 10^5$ for 90° airfoil. The blockage ratio of the model in the test section was about 6%; hence, the wall effects were negligible [32]. The loss distribution at lateral sections of the downstream flow was determined using a rake of total pressure probes. The rake is composed of pitot tubes parallel to one another and has a clearance of 6 mm (Figure 5).

A traverse mechanism with a resolution of 0.1 mm has been used to move the rake holder longitudinally and laterally inside the test section. The stations of data collection were chosen to capture the flow structure variations from near to far wake region of the downstream flow. According to the array of splitting airfoils' intended function as a novel distortion generator design in an engine ground test mechanism, the flow structure and loss distribution at the stations in the far wake region are more critical than the loss distribution directly behind the array. The lateral step of the rake scroll at each station was set to
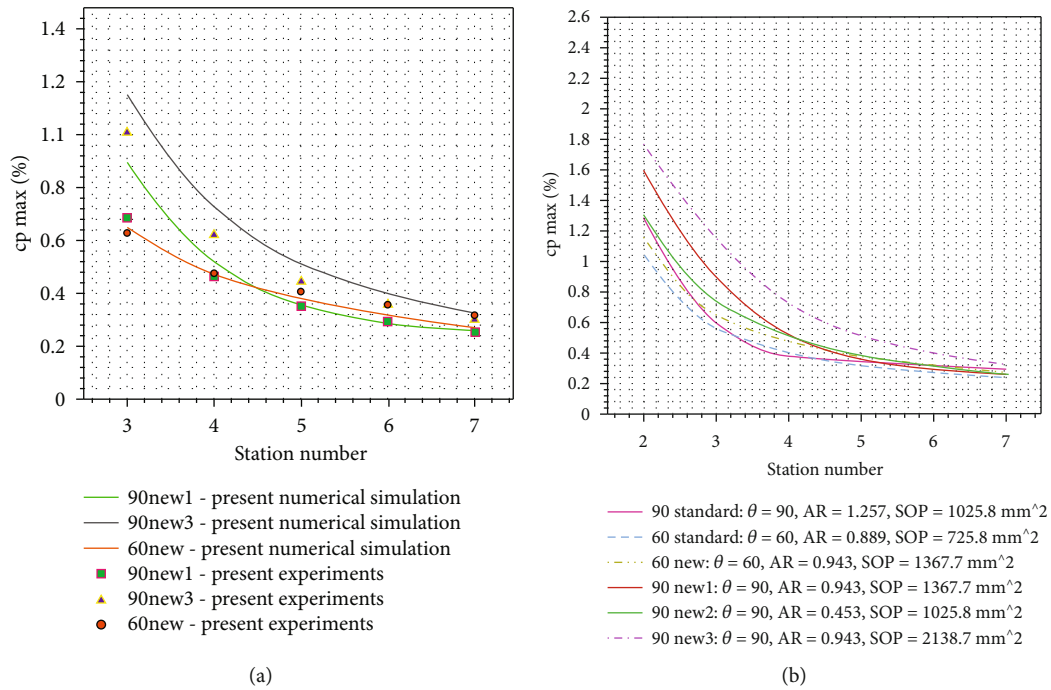
(a)

(b)

FIGURE 6: Max cp values at different stations. (a) Comparison of test and simulation results. (b) Comparison of standard and modified airfoils values obtained from the present numerical simulation.
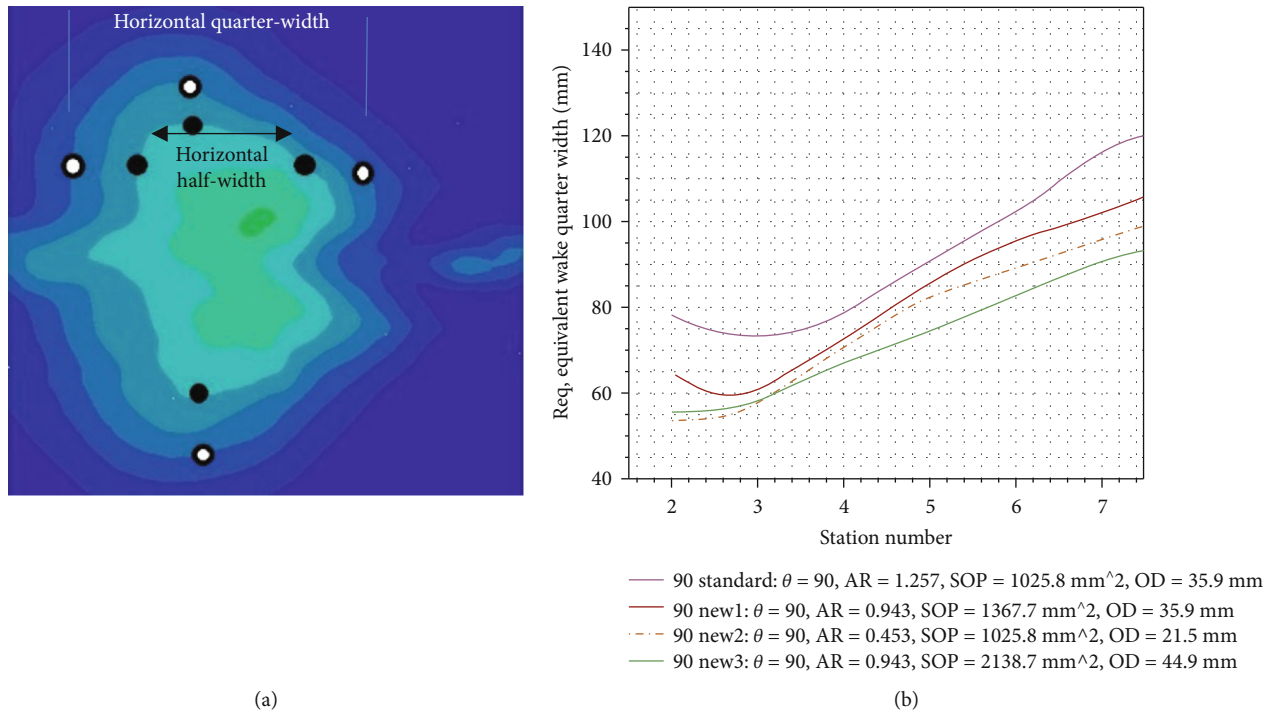

(a)

(b)

FIGURE 7: (a) Illustration of hollow points "○" used to define quarter-width vs. solid points "●" used for half-width. (b) Comparison of the equivalent wake quarter-width variations at different stations for modified and standard 90° airfoils.

6 mm, matching the probe spacing on the rake so that data collection occurred essentially on nodes of a grid with square cells. This imaginary grid with 6 mm cells was termed the "data collection grid." In experiments with single wedges, Eddy Jr. [14] analyzed the probe's traverse distances of 6.35 and 3.17 mm. The study weighed the cost-benefit of contour accuracy and the number of needed lateral stations and concluded that a distance of 6.35 mm was the better choice. This was used to determine the cell size for data collection grid.
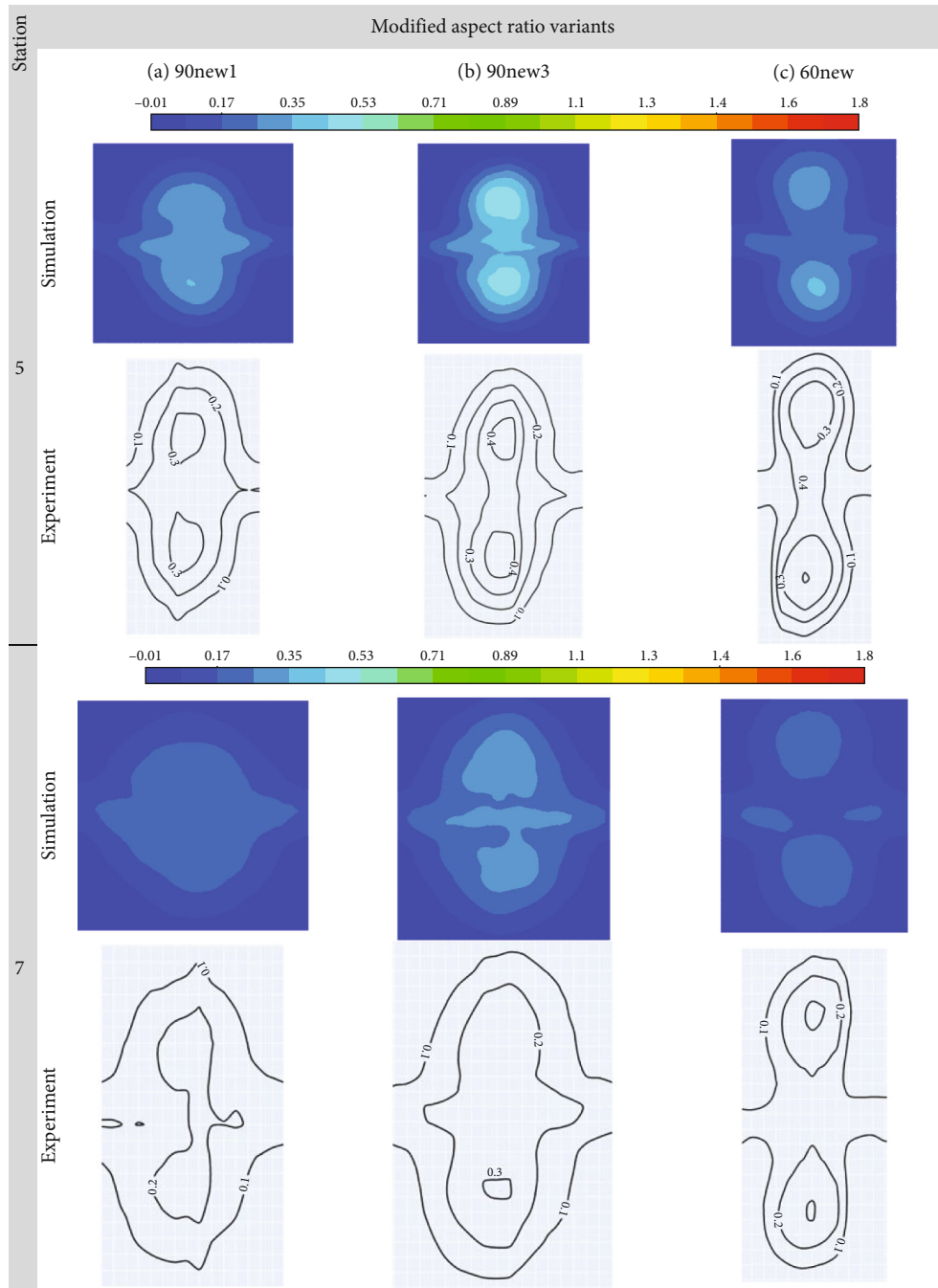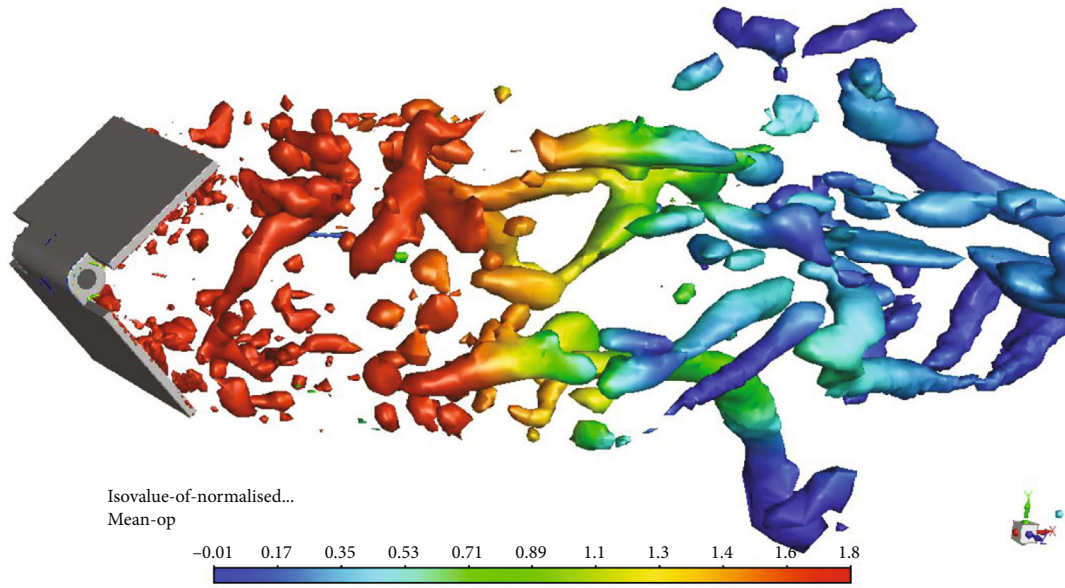
FIGURE 8: Comparison of wind tunnel and simulation results for cp distribution at stations 5 and 7 for 3 modified aspect ratio variants (a) 90new1, (b) 90new3, and (c) 60new.
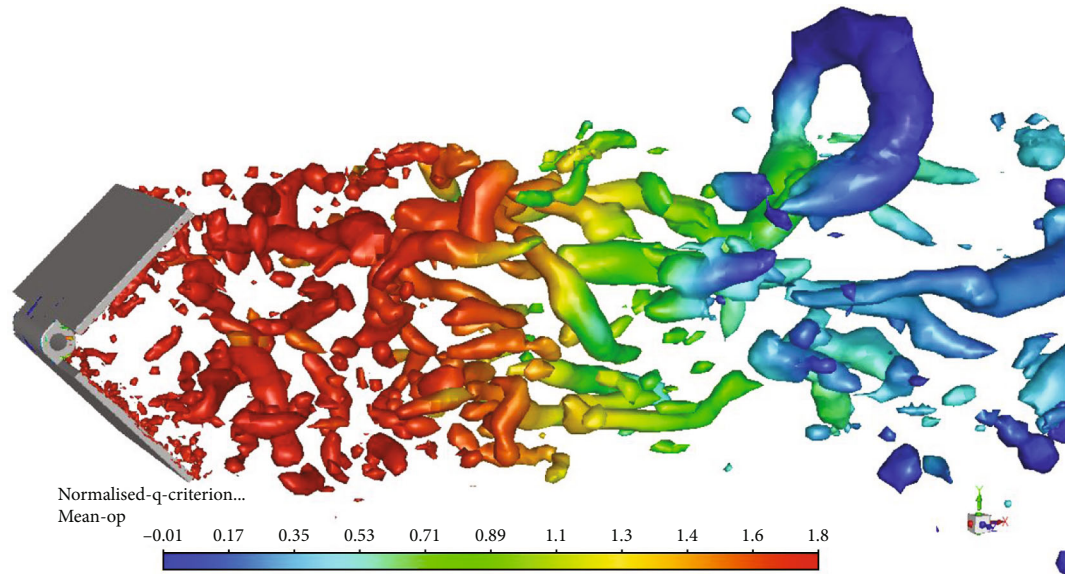
The splitting airfoils were fabricated using additive manufacturing as two separate plates of a thermoplastic material. After they are positioned on the axis (Figure 5(b)), it would be possible to adjust the desired wedge angle. Nut screws were used to secure the plates at a specific angle to the steel axis. The wedges axis was fixed at specific position using a slotted annular stand, as shown in Figure 5(a). All total pressure probes were connected to one of the channels of differential pressure transducers via

flexible tubes; the other channel of sensors was connected to a pitot tube installed upstream of the airfoil(s).

DC005NDC4 Honeywell transducers with operating pressure ranges of ±5 in. H2o, a maximum sampling rate of 2.5 kHz, and the accuracy of 0.2% FSO were used to determine the total pressure at various stations. The sensor's output voltage is connected to a 16-bit 6032 E National Instrument data acquisition card. To eliminate the undesirable effects of momentary pressure fluctuations caused by

Isovalue-of-normalised...
Mean-op

−0.01 0.17 0.35 0.53 0.71 0.89 1.1 1.3 1.4 1.6 1.8

(a)

Normalised-q-criterion...
Mean-op

−0.01 0.17 0.35 0.53 0.71 0.89 1.1 1.3 1.4 1.6 1.8
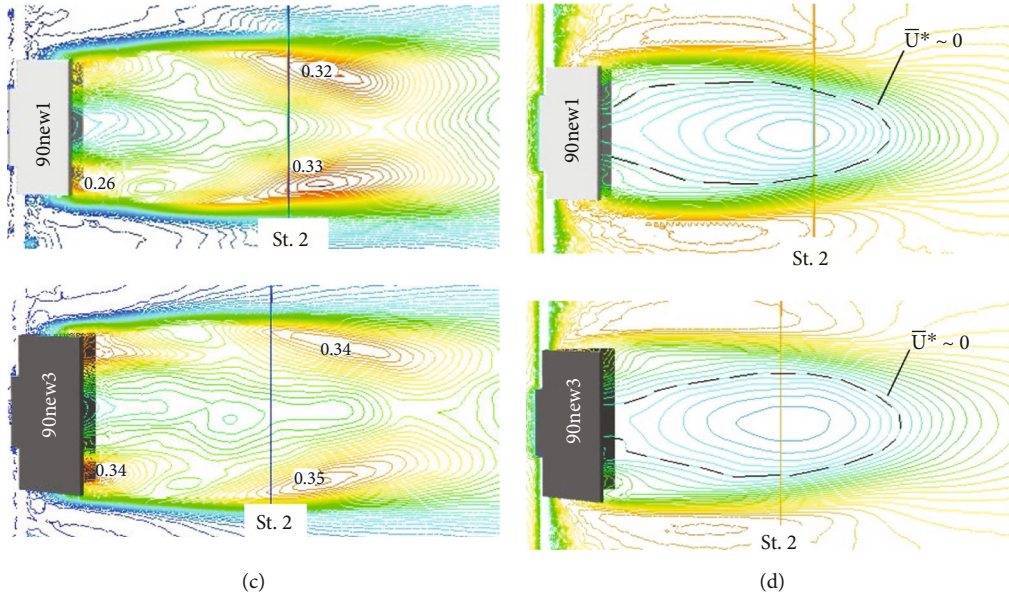
(b)

Figure 9: Continued.

(c)

(d)

FIGURE 9: Isosurface of normalized Q – criterion = 0.1 colored by mean cp: (a) 90new1 and (b) 90new3. (c) Comparison of u^*_{rms} distribution. (d) Comparison of $\bar{U}^*$ distribution.

turbulence in the free stream flow within the test section, as well as possible noise in the acquisition mechanism, data were collected at a rate of 2500 samples per second every 5 seconds, and the resulting values were averaged and reported.

The uncertainty associated with total pressure measurements is due to various sources summarized in Table 2. The overall uncertainty of normalized Pt differences (between the array's upstream and downstream) measured by pressure transducers is approximately 3.38% [33].

3. Results and Discussions

3.1. Effects of Aspect Ratio and opposite Surface. Figure 6(a) illustrates cp_{max} values at different stations (for selected modified wedges) obtained from the present simulation and is compared with the present test results. Comparison of the curves demonstrates a good agreement between the results especially as the flow approaches the fully developed region. Numerical simulations overpredict the loss coefficient up to 12% for stations at the near wake region. The determining factors on the loss distribution at near wake region are wedge sizes and consequently recirculation zone size. As observed in Figure 6(b), 90new3 (with the biggest S_{op}) generates the greatest cp_{max} at station No. 2 and 3. In the same behavior, 90new2 and 90-standard airfoils with the equal S_{op} produce equal cp_{max}. As the flow moves downstream, the cp curve trend depends on the airfoil's aspect ratio. 90new2 airfoil with the smallest AR acts in this way that the flow separation from above and bottom points determines the flow structure at all stations. Consequently, the flow has a 2D structure, and the loss coefficient reduction trend is uniform and quasilinear. On the opposite side is the 90-standard wedge with the biggest aspect ratio that the cp

curve shows the maximum slope change in passage from the stations. As mentioned in the computational grid considerations, the primary characteristic of 90° airfoil downstream flow is the predominance of three-dimensional effects, due to the side separation led to the wake axis switching.

Transverse flow over the wedge surface is possible as it escapes from the side edges plus above and below regular separation points. Thus, in contrast to the AR < 1 airfoils category, the velocity recovery, and wake-freestream synchronization processes occur in a fully three-dimensional manner. This phenomenon results in a faster recovery rate and a more intense rate of cp reduction (between stations 2 and 5). In other words, the slope of the cp curve is affected and exhibits a distinct concavity. It should be noted that the amount of fluid entrained from the free stream into the wake zone directly correlates with the degree of velocity recovery during the wake development process [34]. For 90new1 and 90new3 wedges, the loss coefficient reduction rate in passage from the stations is something between 90new2 and 90-standard. To put it differently, the reduction rate of cp is directly related to the airfoil aspect ratio and consequently the flow separation form. An interesting feature that is observed in the chart is the proximity or coincidence of the cp_{max} values associated with the various AR variants at station 7. Eddy Jr.'s [14] tests on single airfoils revealed that the cp values are very close to one another at st.7, indicating an approach to the similarity or far wake region (where the wake is fully developed) [35].

Figure 7 illustrates the equivalent wake quarter-width "R_{eq}" concept and its variations at different stations for modified and standard 90° airfoils. The distance between two points on a (horizontal/vertical) line of cp contour that passes through the area of maximum loss and has a cp value
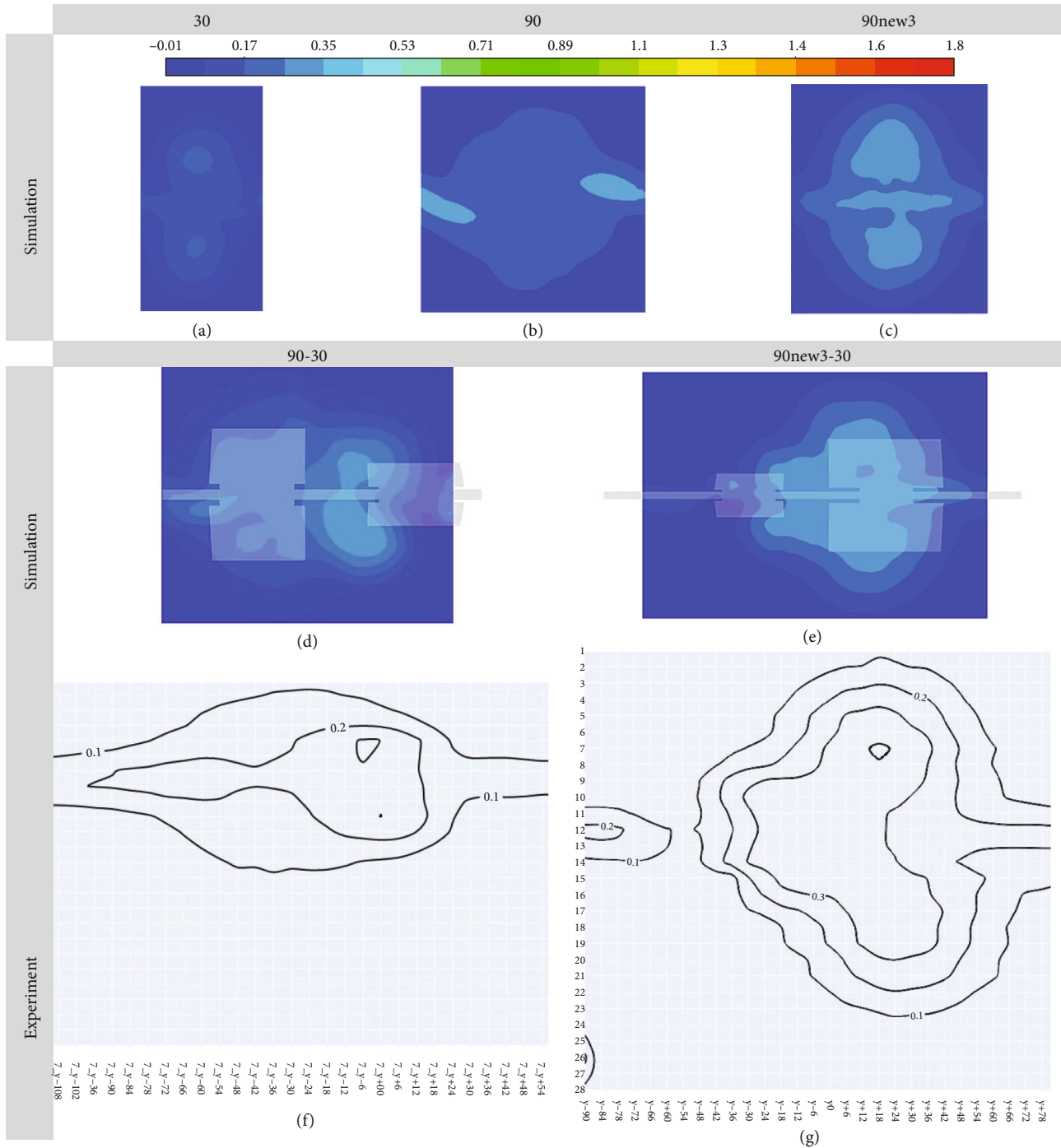
FIGURE 10: Comparison of the combined wake pattern at station 7 obtained from the present wind tunnel tests and numerical simulation for 90-30 and 90new3-30 arrangements besides the single patterns.

equal to a quarter of the cp_{max} is referred to as the "quarter-width." The a and b parameters in Equation (8) are horizontal and vertical "quarter-width."

$$R_{eq} = \sqrt{a \times b}. \tag{8}$$

Mutter [36] pioneered the concept of "half-width" in his research on elliptical jets. The authors of the present study

concluded from their examination of the loss pattern and half-width calculation that the calculated R_{eq} based on half-width provided an estimate of the wake section size at the central core; thus, the sensitivity of the parameter (R_{eq}) to the change in outer size is insufficient. As depicted in Figure 7(a), the authors recommend using the term "quarter-width" rather than "half-width" to encompass a larger pattern area, which makes the dimensions more
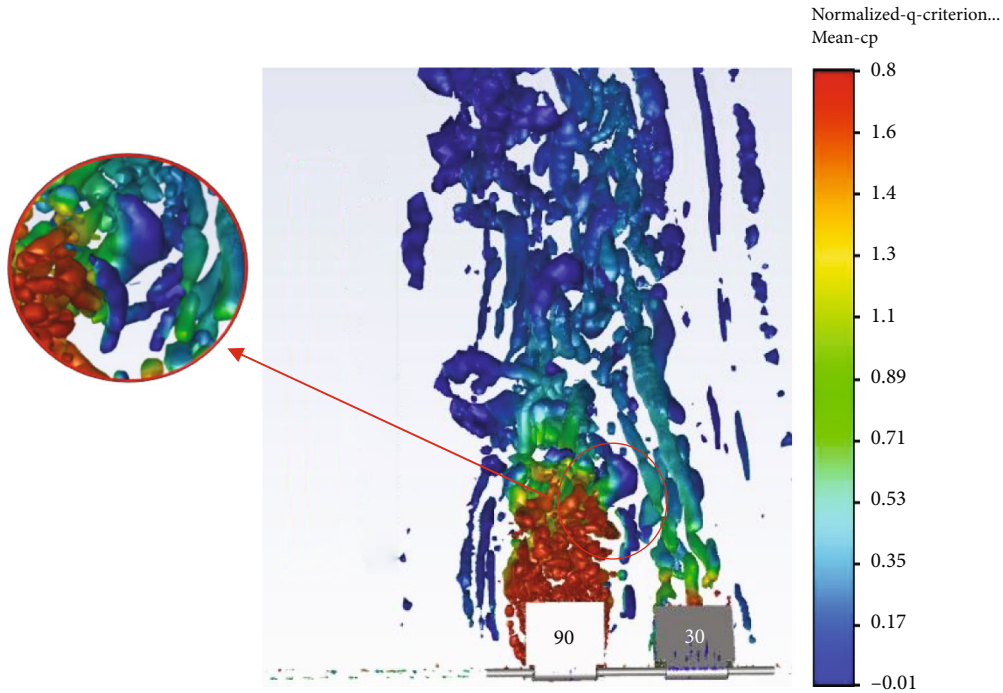
(a)
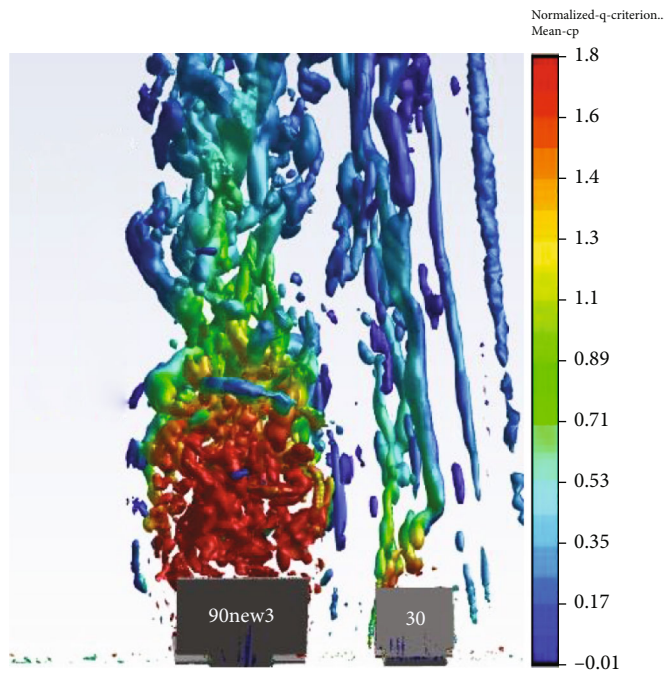
(b)

FIGURE 11: Comparison of combined flow structures for 90-standard and 90new3 dual arrangements with 30° wedge at the same CW in the form of normalized Q − criterion = 0.1 isosurface colored by mean cp.

tangible. As observed, the curve of R_{eq} for 90-standard airfoil (with maximum AR) shows the maximum slope change in passage from the stations (similar to cp curve). To put it simply, the modified airfoil R_{eq} variation curve demonstrates a more quasilinear behavior with the reduction of aspect ratio. It seems that the 90new3 airfoil with this advantage

and the bigger cp at far wake region (due to the greater S_{op}) is superior to the others according to the predictability of multiple arrangement loss.

Distribution of the total pressure loss coefficient at 2 selected downstream stations near far wake region for 3 modified aspect ratio variants are presented in Figure 8.

The total pressure differences $(P_{t\,\max} - P_t)$ measured at the data collection grid nodes in present wind tunnel tests normalized by $P_{t\,\max}$ are presented as cp isolines. As observed, the isoline pattern and loss distribution are compared well with colored cp contours obtained from the present numerical simulations. Delaying of the wake axis switching as the intended purpose of the aspect ratio reduction is clearly visible in the loss patterns at station 7 for 90new1 and 90new3 airfoils relative to 90-standard airfoil loss pattern depicted in Figure 3. In other words (for modified airfoils downstream flow), the vertical pattern of maximum loss lobes extended to the boundary of fully development at station 7 that is a constructive factor in prediction of the combined wake pattern of airfoils arrangement from single patterns. In this sense, 90new3 demonstrates a more consistent behavior like the trend of $cp_{\max}$ curve. It is seen that aspect ratio reduction applied to 90° airfoil provides a higher level of loss related to AR > 1 airfoil category along with the quasi-2D behavior of separation pattern (regular separation pattern from top and bottom edges and the elimination of side separation) related to AR < 1 airfoils category.

Figure 9 presents the isosurfaces of the normalized Q-criterion (Norm. $Q = 0.1$) colored by time-averaged cp values for 90new1 and 90new3 airfoils. The Q criterion and the concept of the velocity gradient tensor "D_{ij}" are used to identify vortices in turbulent flow fields, with the vortex assumed to be a continuous flow region with a positive Q [37].

$$D_{ij} = S_{ij} + \Omega_{ij},$$
$$Q = \frac{1}{2} \left\| \bar{\Omega} \right\|^2 - \left\| \bar{S} \right\|^2. \qquad (9)$$

The Q parameter indicates the extent to which vorticity "Ω" prevails over the strain rate "S"; thus, a larger Q value indicates a stronger vortex. Figures 9(a) and 9(b) indicate more 3D structure in the near wake region of 90new3 relative to 90new1 that demonstrates more three-dimensional vortices in this zone of 90new3 downstream flow. Also, the existence of larger 3D structures while moving downstream is the indicator of larger vortex formation. This is observed in the other form in parts (c) and (d) of the present figure. The root mean square of the x velocity fluctuations relative to the freestream velocity denoted by "u^*_{rms}" indicates vortex power; the location of its maximum value indicates the roll-up position of the shear layer, and the distance between this position and the airfoil axis indicates the vortex formation length scale "L_f" [38, 39]. "$\bar{U}^*$" isolines also were plotted to define the recirculation zone, as shown in part (d). The isoline corresponding to $\bar{U}^* = 0$ defines the boundaries of the recirculation zone [18]. As observed, the 90new3 airfoil downstream flow with the bigger recirculation zone which is extended beyond station 2 demonstrates more powerful vortices with the higher values of u^*_{rms}.

It is seen that 90new1 and 60new airfoils with equal AR and S_{op} indicate different cp values to the intermediate stations. To put it simply, the opening angle of airfoil is another factor that affects the separation pattern of flow. As a result, the 90new1 generated the greater loss coefficient at the men-
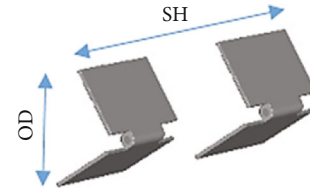

FIGURE 12: Geometric parameters of the airfoil arrangement used to calculate the characteristic width "CW."

tioned stations. In general, the modified AR variants loss distribution studies led to the selection of the 90new3 airfoil for multiple arrangement by the authors, due to more pronounced characteristics of repeatability and predictability.

3.2. Multiple Arrangement Using Selected Modified Airfoil. As stated in Ref. [40], with a view to the predictability of airfoils combined loss pattern, the horizontal spacing studies between 90° and 30° wedges demonstrated that the maximum value of spacing equals to 19.05 mm is the best among studied values. In order to compare the effects of aspect ratio reduction on loss distribution generated by the airfoils horizontal arrangement, the combined wake pattern of modified and standard 90° wedge at station 7 with mentioned spacing is illustrated in Figure 10. When the experimental and numerical isocontours are compared, an excellent agreement is observed. In other words, the figure demonstrates the numerical simulation's superior performance in predicting the combined loss "pattern," for modified airfoil. The contours indicate that the complexity of combined wake section and its tendency to 30° wedge (depicted in part (d) of the figure) due to the "side separation" of 90-standard wedge was eliminated in 90new3-30 arrangement. This is a result of modified 90° wedge width elongation effects on the separation structure. Unlike in the 90-standard that side separation is a determining factor especially after intermediate stations, the main part of the 90new3 upstream flow separates from upper and lower edges of airfoil. Consequently, correction of the maximum loss lobes positioning and its destructive effects on combined pattern repeatability relative to singles is obtained. To put it differently, continuation of 90new3 wake axis vertical positioning at station 7 like 30° wedge led to appreciable improvement of the combined loss pattern predictability. This feature is clearly visible in discrete downstream flow structure of 90new3-30 dual layout compared to the intertwined structure of 90-30 dual arrangement downstream flow in Figure 11. Large 3D structures (isosurfaces of the normalized Q) in the gap region of the latter layout demonstrate the strong vortex formation. In order to generalize the airfoils spacing studies, 2 normalized parameters are introduced according to Equation (10) and Figure 12. In which OD_MAIN is the opposite diameter of the airfoil with greater opening angle that is called "main airfoil." The characteristic width was equal to 2.2 for both arrangements of Figure 11.

$$CW = \frac{SH}{OD\_MAIN},$$

$$SD = \frac{\text{Distance from the station to the airfoil axis}}{OD_{MAIN}}. \qquad (10)$$
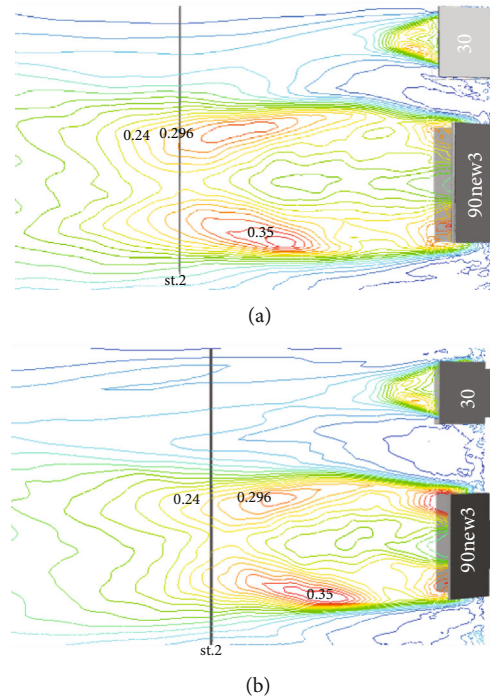
(a)

(b)

FIGURE 13: Comparison of u^*_{rms} distribution for 90new3-30 arrangements with 2 different characteristic widths: (a) CW = 2.12 and (b) CW = 2.4.

Airfoil spacing increasing effects study conducted on the selected modified airfoil multiple layouts. The results demonstrated that the cp_{max} magnitude is dominated by the main airfoil in the arrangement. Figure 13 shows the distributions of u^*_{rms} for 2 different characteristic widths. The size and position of 0.296 isoline relative to st.2 line indicate that increasing the airfoils distance (the greater CW in part b) reduces the power of the strongest vortices by accelerating their decay process in the gap shear layers. This behavior of the gap flow is conforming to the findings of Alam et al. in Ref. [18] for a similar bluff body.

Figure 14 presents the equivalent wake quarter-width "R_{eq}" variations at downstream stations for 3 different "CW." As observed, the curves represent a more quasilinear trend for greater characteristic width that confirms the reduction process of the combined wake pattern complexity. This characteristic is a helpful factor to predict the combined loss distribution.

Figure 15 shows the downstream wake sections of 90new3-30 horizontal layout in the form of time-averaged cp isolines at the stations located in fully developed wake region. The isolines obtained from numerical simulations performed on arrangements for 4 different characteristic widths. It is observed that the minimum CW leads to the same cp_{max} as single 90new3 equals to 2.4. In other words, the minimum distance of second airfoil relative to the main airfoil should be equal to 2.4 times OD_MAIN to decrease the combined loss and achieve the same magnitude of maximum loss coefficient as the single wedge. Figure 16 illustrates a hypothesis proposed by the present research authors. It seems that loss distribution from single pattern to triple wedges pattern at SD = 9.6 follows
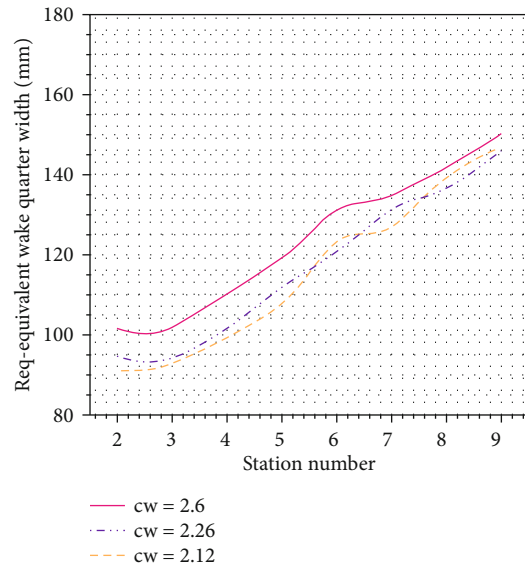

FIGURE 14: Equivalent quarter-width variations at different stations for 3 characteristic widths.

a hierarchical process. To put it simply, airfoils' triple layout loss pattern can be predicted from dual arrangement pattern, and the latter can be predicted from single airfoil loss distribution. Accordingly, the loss distribution of 90new3 dual and triple arrangements with 30° wedge at SD = 9.6 has been indicated in the figure. It can be seen that the combined c p_{max} of dual and triple layouts with CW = 2.4 is similar to the single one and equals to 0.17.
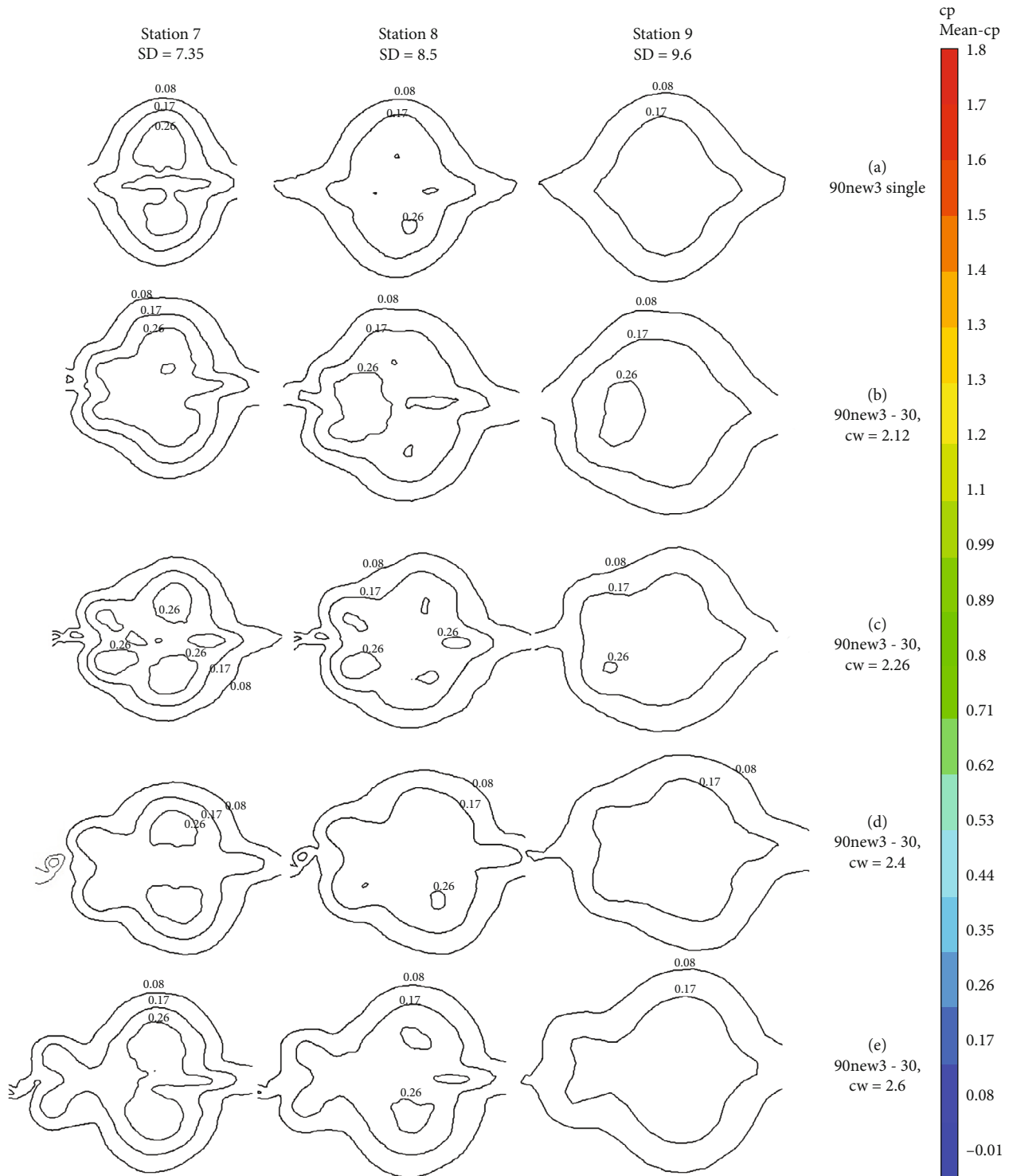
FIGURE 15: Loss distributions in the form of time-averaged cp isolines at the stations located in fully developed wake obtained from present numerical simulations. (a) 90new3 single and 90new3-30 spacing equal to (b) CW = 2.12, (c) CW = 2.26, (d) CW = 2.4, and (e) CW = 2.6.

Figure 17 compares cp isolines for the studied arrangements of selected modified wedge obtained from loss measurements performed in the present wind tunnel tests with the simulation results depicted in Figures 15 and 16. The figure demonstrates a good numerical prediction for the com-

bined loss "pattern." Regarding the maximum combined "loss value," it is seen that the numerical simulation overpredicts the velocity recovery rate, and the wake-freestream synchronization processes in fully developed region at SD = 9.6. In other words, small zones of greater loss can be
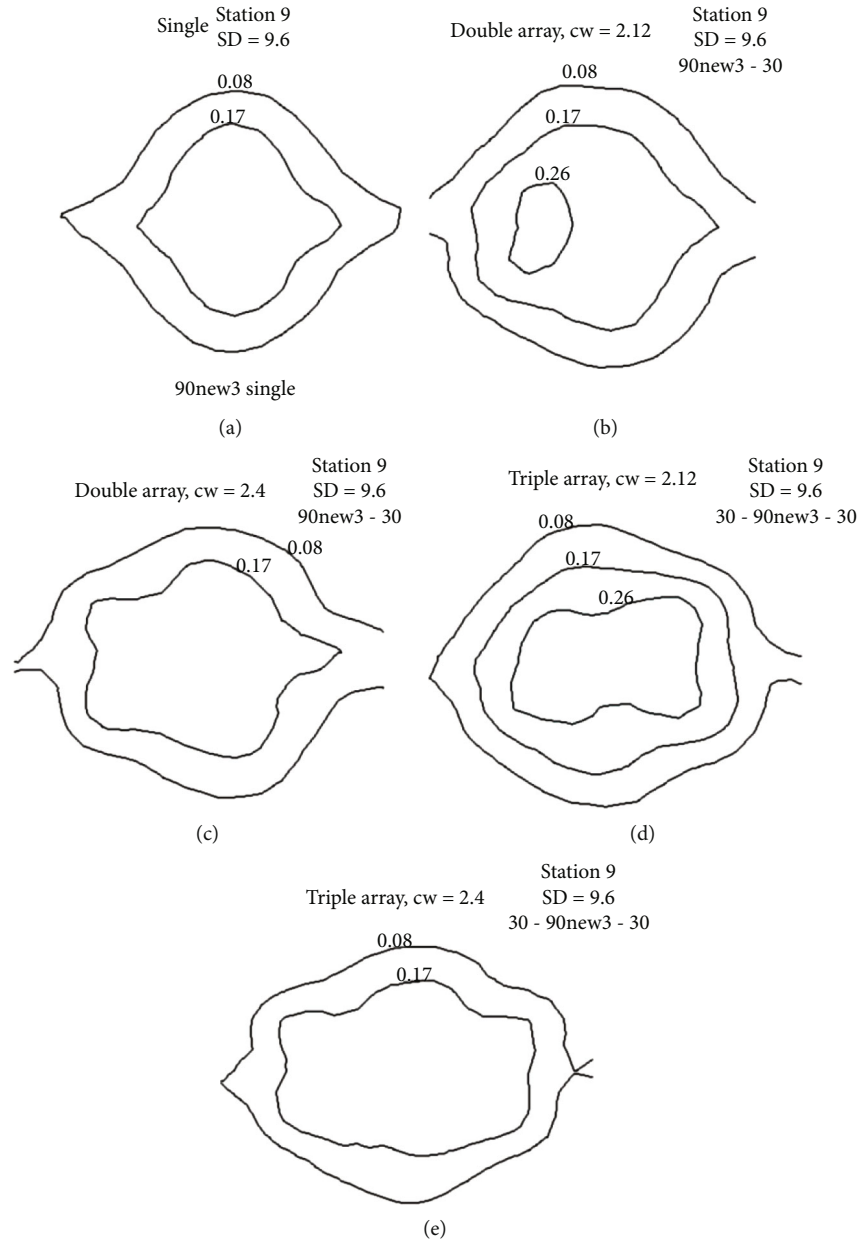
FIGURE 16: Illustration of the hierarchical process hypothesis in loss distribution from a single pattern to triple wedges pattern.

observed in experimental results at the mentioned SD which is not found in simulation results.

Intended function of the airfoils array as the distortion generator demands the expansion of created loss zones at some regions, according to the recognized loss distribution at the reference inlet-engine interface plane. The mentioned expansion of lobes in the determined loss distribution can be obtained by using the greater opening angle and characteristic width in the splitting airfoils arrangement. As observed in the loss distributions of Figure 17, the characteristic width equals to 2.6 at a depicted pattern in part (d2) of the figure represent the same cp_{max} magnitude as CW = 2.4 and at a showed pattern in part (c2) with the slightly larger lobes of

loss. The 60° and 30° wedges were used in the former and latter layouts, respectively.

In general, it can be expressed that the proposed hierarchical process hypothesis in loss distribution of the airfoils array is confirmed to high extent. According to the present analysis, the character of array composed of multiple splitting airfoils will be recognizable.

Figure 18 shows the effects of CW on the equivalent wake quarter-width (R_{eq}) of 90new3 and 30° airfoils triple arrangements at different downstream stations. As observed, characteristic width increment does not affect the slop of the curves of triple arrangements. In other words, the rate of equivalent width increments along downstream stations
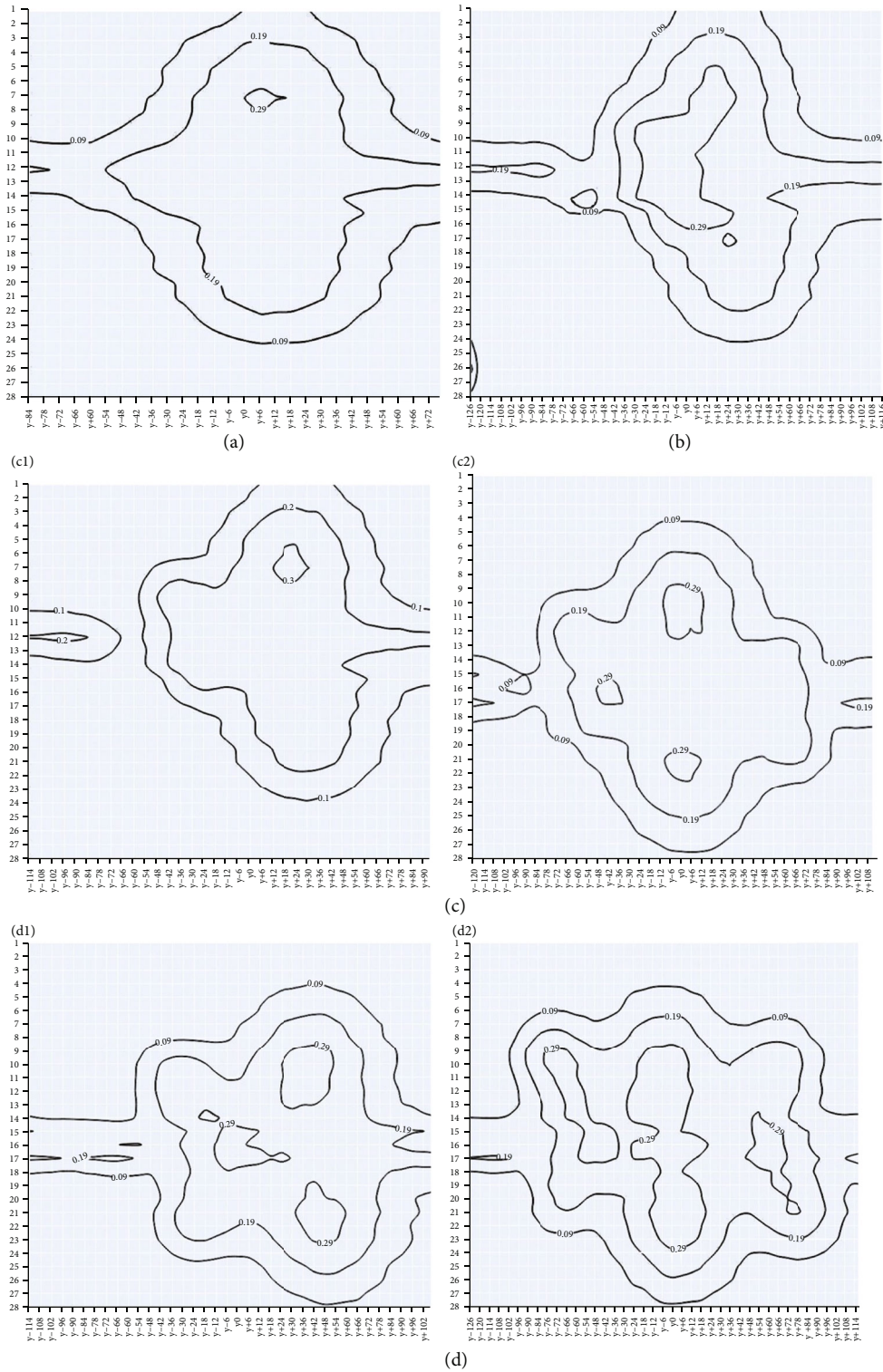
Figure 17: Loss distributions in the form of cp isolines at SD = 9.6 obtained from present wind tunnel measurements. (a) 90new3 single. (b) 90new3-30, CW = 2.12. (c1) 90new3-30 dual. (c2) 30-90new3-30 triple layouts with CW = 2.4. (d1) 90new3-60 dual. (d2) 60-90new3-60 triple layouts with CW = 2.6.
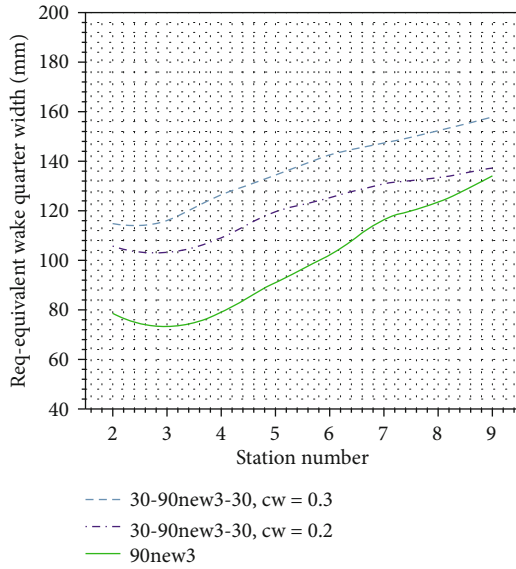
FIGURE 18: Illustration of CW effects on R_{eq} variations for 2 triple arrangements of 90new3 with 30° airfoils.

according to the determined CW remains approximately constant. However, both triple arrangements demonstrate a reduction in the curve slope relative to the single and dual layouts (Figure 14). To put it differently, for the "30-90new3-30" triple layout, the wake size increment rate is less than the rates related to the 90new3-30 dual and 90new3 single layouts.

4. Conclusion

Improvement of the predictability of loss distribution due to the splitting airfoils array was the intended purpose of the present research. Extensive numerical simulations based on the DDES hybrid turbulence model were conducted on 90° airfoil variants to study the feasibility of downstream flow structure correction. Modified aspect ratio (AR) variants with different reduced ARs and opposite surfaces (S_{op}) were studied in the single and combined arrangements. In order to validate the simulation results, total pressure loss experimental isolines were extracted from wind tunnel measurements using the rake of pitot tubes at the selected sections of the downstream flow. Comparison of numerical and experimental results has shown the following:

The wake axis switching as a destructive factor for prediction of the multiple arrangement loss distribution (had been captured for 90° standard airfoil) is weakened and delayed in moving downstream due to the reduction of aspect ratio below the limiting value of "1."

As another constructive result of aspect ratio reduction that is helpful to predict the loss behavior of the airfoil, a quasilinear trend is observed in the curve of maximum loss coefficient at different stations due to the regular separation pattern (from top and bottom edges) and the elimination of side separation. The equivalent wake quarter-width "R_{eq}" variation curves demonstrate a similar trend. To put it Sim-

ply, R_{eq} as a representative parameter of the wake size has a relatively constant increase rate (for modified AR variants) approaching far wake region.

Increasing the opposite surface of the wedge with the determined AR and opening angle lead to the formation of more 3D flow structures (just behind the body), larger recirculation zone, and stronger vortices with the longer formation length in near wake region.

A hierarchical process can be observed in the loss distribution from single modified wedge pattern to triple wedges combined loss pattern including it. In other words, loss pattern of the triple arrangement of the airfoils can be reconstructed from dual arrangement, and it can be reproduced from single splitting airfoil pattern.

Numerical simulations are less accurate in the prediction of the "maximum loss magnitude" and velocity recovery rate at fully developed region of the arrangement downstream flow relative to " loss pattern."

Predictability of the airfoils horizontal arrangements including modified AR variants of 90° airfoil is improved. This is because the persistence of the maximum loss lobes positioning and elimination of their rotation lead to reduction of the complexity of combined flow structure.

Symbols

AR:	Splitting airfoil aspect ratio (opposite diameter to width)
a and b:	Horizontal and vertical quarter-width
cp:	Total pressure loss coefficient
CW:	Characteristic width of the airfoils' arrangement
D:	Characteristic length scale
DES:	Detached Eddy simulation
DDES:	Delayed detached Eddy simulation
E:	Turbulence energy spectrum
f:	Vortex shedding frequency
FSO:	Full-scale output
GR:	Growth rate of computational grid nodes spacing
k:	Turbulent kinetic energy
K:	Frequency proportional to vortex characteristic size
LES:	Large Eddy simulation
OD:	Splitting airfoil opposite diameter
$P_{t\ max}$:	Maximum total pressure at the upstream of the airfoil(s)
P_t:	Local total pressure at downstream
L_f:	Vortex formation length
RANS:	Reynolds-averaged Navier-Stokes
R_{eq}:	Wake equivalent width
Re_{OD}:	Reynolds number based on OD
S:	Strain rate tensor
SD:	Nondimensional distance from the airfoil(s) axis
s:	Splitting airfoil width
SGS:	Subgrid scale
SRS:	Scale-resolving simulation
S_{op}:	Opposite surface of airfoil perpendicular to flow
t:	Total condition
St:	Strouhal number

u_{rms}^*:   Streamwise velocity fluctuation normalized by freestream velocity

U: Freestream velocity

$\bar{U}^*$:   Time-averaged streamwise velocity normalized by freestream velocity

Ω: Vorticity tensor

τ: Time required to scroll the computational domain with the selected time step

τ_{ij}:   Stress tensor

Data Availability

The experimental and numerical data used to support the findings of this study are included within the article.

Conflicts of Interest

The authors declare that they have no conflicts of interest.

References

[1] Society of Automotive Engineers (SAE), *Inlet Total-Pressure-Distortion Considerations for Gas-Turbine Engines*, SAE International, United States, 2017, Aerospace Inf. Report No: AIR 1419c.

[2] M. Davis, W. Baker, G. Power, and D. Beale, "A proposal for integration of wind tunnel and engine test programs for the evaluation of airframe-propulsion compatibility using numerical simulations," *Journal of Engineering for Gas Turbines and Power*, vol. 124, no. 3, pp. 447–458, 2002.

[3] M. Sivapragasam, "Flow field behind a complex total pressure distortion screen," *Proceedings of the Institution of Mechanical Engineers, Part G: Journal of Aerospace Engineering*, vol. 233, no. 14, pp. 5075–5092, 2019.

[4] K. Song, B. Zhao, H. Sun, and W. Yi, "A physics-based zero-dimensional model for the mass flow rate of a turbocharger compressor with uniform/distorted inlet condition," *International Journal of Engine Research*, vol. 20, no. 6, pp. 624–639, 2019.

[5] A. P. Farr, "Evaluation of F-15 inlet dynamic distortion," *Journal of Aircraft*, vol. 13, no. 1, pp. 36–42, 2012.

[6] G. McLelland, D. G. MacManus, P. K. Zachos, D. Gil-Prieto, and M. Migliorini, "Influence of upstream total pressure profiles on S-duct intake flow distortion," *Journal of Propulsion and Power*, vol. 36, no. 3, pp. 346–356, 2020.

[7] D. Beale, K. Cramer, and P. King, "Development of improved methods for simulating aircraft inlet distortion in turbine engine ground tests," in *22nd AIAA Aerodynamic Measurement Technology and Ground Testing Conference*, p. 3045, Missouri, USA, 2002.

[8] J. Seddon and E. L. Goldsmith, *Intake Aerodynamics*, vol. 2, Oxford: Blackwell science, 1999.

[9] J. L. Younghans, M. T. Moor, T. P. Collins, and J. G. Direnzi, "Inlet flow field simulation techniques for engine/compressor testing," *Aircraft Engineering and Aerospace Technology*, vol. 591, 1970.

[10] G. R. Lazalier and J. T. Tate, "Development of a prototype discrete frequency, total-pressure fluctuation generator for jet engine/inlet compatibility investigation," *Proc. Air Force Airframe Propulsion Compatibility Symposium, AFAPL-TR AFAPL-TR: Air Force Aero Propulsion Lab Technical Report*, vol. 69-103, pp. 517–549, 1970.

[11] P. H. Kutschenreuter, T. P. Collins Jr., and W. F. Vier, "The P3G-a new dynamic distortion generator," *Journal of Aircraft*, vol. 11, no. 6, pp. 344–348, 1974.

[12] T. DiPietro, *Fundamental Wind Tunnel Experiments for Total Pressure Distortion Generator Concept Selection*, Year-End Report for Sverdrup Technology, 1996.

[13] J. Jumel, P. S. King, and W. F. O'Brien, *Transient Total Pressure Distortion Generator Development, Phase II, Final Report for Academic Qualification [M.S. thesis]*, Virginia Polytechnic Institute and State University, Blacksburg, VA, 1999.

[14] G. L. Eddy Jr., *Study of Steady-State Wake Characteristics of Variable Angle Wedges, [M.S. thesis]*, Virginia Polytech. Institute and State Univ, Blacksburg, Virginia, 2001.

[15] Ansys Inc, "Ansys fluent, Release 19.0, help system, theory guide, chapter 4 and user's guide, chapter 28," 2018.

[16] A. Prasad and C. H. K. Williamson, "The instability of the shear layer separating from a bluff body," *Journal of Fluid Mechanics*, vol. 33, pp. 375–402, 1997.

[17] G. S. Cardell, *Flow Past a Circular Cylinder with a Permeable Splitter Plate, [Ph.D. Thesis]*, California Institute of Technology, Pasadena, 1993.

[18] M. M. Alam, Y. Zhou, and X. W. Wang, "The wake of two side-by-side square cylinders," *Journal of Fluid Mechanics*, vol. 669, pp. 432–471, 2011.

[19] H. L. Bai and M. M. Alam, "Dependence of square cylinder wake on Reynolds number," *Physics of Fluids*, vol. 30, no. 15102, pp. 1–19, 2018.

[20] P. Ausoni, *Turbulent Vortex Shedding from a Blunt Trailing Edge Hydrofoil, [Ph.D. Thesis]*, Ecole Polytechnique Federal, Lausanne, Switzerland, 2009.

[21] P. Bjswe, B. Johnson, and B. Phinney, *Optimization of oscillating body for vortex-induced vibrations*, Worcester Polytechnic Institute, 2011, E-project-042811-120045.

[22] Z. J. Taylor, *Vortex shedding from elongated bluff bodies, [Ph.D. Thesis]*, University of Western Ontario, 2011.

[23] A. Roshko, "Experiments on the flow past a circular cylinder at very high Reynolds number," *Journal of Fluid Mechanics*, vol. 10, no. 3, pp. 345–356, 1961.

[24] B. Cantwell and D. Coles, "An experimental study of entrainment and transport in the turbulent near wake of a circular cylinder," *Journal of Fluid Mechanics*, vol. 136, no. 1, pp. 321–374, 1983.

[25] P. Spalart, S. Deck, M. Shur, K. Squires, M. Strelets, and A. Travin, "A new version of Detached-eddy simulation, resistant to ambiguous grid densities," *Theoretical and Computational Fluid Dynamics*, vol. 20, no. 3, pp. 181–195, 2006.

[26] B. Wang, J. Liu, Y. Yang, and Z. Xiao, "Numerical studies of undulation control on dynamic stall for reverse flows," *Acta Mechanica Sinica*, vol. 36, no. 2, pp. 290–305, 2020.

[27] F. R. Menter, *Scale-Resolving Simulations in ANSYS CFD*, ANSYS Germany H, Technical report version 1, Darmstadt, Germany, 2012.

[28] P. R. Spalart, "Strategies for turbulence modelling and simulations," *International Journal of Heat and Fluid Flow*, vol. 21, no. 3, pp. 252–263, 2000.

[29] J. Smagorinsky, "General circulation experiments with the primitive equations," *Monthly Weather Review*, vol. 91, no. 3, pp. 99–164, 1963.

[30] F. R. Menter and M. Kuntz, "Adaptation of Eddy-viscosity tur-bulence models to unsteady separated flow behind vehicles," in *The Aerodynamics of Heavy Vehicles, Trucks, Buses and Trains*, Springer, Asilomar, Ca, 2003.

[31] M. S. Gritskevich, A. V. Garbaruk, J. Schütze, and F. R. Menter, "Development of DDES and IDDES formulations for the k-ω shear stress transport model," *Flow, Turbulence and Combustion*, vol. 88, no. 3, pp. 431–449, 2012.

[32] G. S. West and C. J. Aplet, "The effects of tunnel blockage and aspect ratio on the mean flow past a circular cylinder with Reynolds numbers between 10000 and 100000," *Journal of Fluid Mechanics*, vol. 114, no. 1, pp. 361–377, 1982.

[33] E. Jorgensen, "How to measure turbulence with hot wire ane-mometer," in *Dantec Dynamics*, pp. 40–44, 2002.

[34] M. M. Alam and Y. Zhou, "The turbulent wake of an inclined cylinder with water running," *Journal of Fluid Mechanics*, vol. 589, pp. 261–303, 2007.

[35] J. A. Schetz, *Foundations of Boundary Layer Theory for Momentum, Heat and Mass Transfer*, Prentice Hall Inc., Englewood Cliffs, NJ, 1984.

[36] T. B. Mutter, *Numerical simulations of elliptical jets*, Virginia Polytechnic University, 1994.

[37] V. Kolar, "Vortex identification: new requirements and limita-tions," *International Journal of Heat and Fluid Flow*, vol. 28, no. 4, pp. 638–652, 2007.

[38] S. M. Bloor, "The transition to turbulence in the wake of a cir-cular cylinder," *Journal of Fluid Mechanics*, vol. 19, no. 2, pp. 290–309, 1964.

[39] J. H. Gerrard, "The mechanics of the formation region of vor-tices behind bluff bodies," *Journal of Fluid Mechanics*, vol. 25, no. 2, pp. 401–413, 1966.

[40] M. Bazazzadeh, M. Hassani, and M. Dehghan Manshadi, "Pre-diction of splitting airfoils horizontal spacing effects on loss distribution in an array distortion generator based on compar-ison of RANS, URANS and DES," *Journal of Solid and Fluid Mechanics*, vol. 11, no. 5, pp. 211–223, 2021.